Journal of Ceramic Processing Research. Vol. 27, No. pp. 1~12 (2026)
(Received 4 2026, Received in revised form 3 2026, Accepted 4 2026)
https://doi.org/10.36410/jcpr.2026.27..

J O U R N A L O F
Ceramic Processing Research

Fabrication of cylindrical - shaped transducer based on $Pb(Zr_{0.525}Ti_{0.475})_{0.970}Nb_{0.024}Sb_{0.006}O_3$ Ceramics and vibration simulation using finite element modeling

Dung Thi Hoai Trang[a], Vo Thanh Tung[a,*], Le Dai Vuong[b], Tran Thanh Van[a], Le Phuoc Dinh[a] and Le Tran Uyen Tu[a]
[a]*University of Sciences, Hue University, Hue City, Viet Nam*
[b]*School of Engineering and Technology - Hue University, Hue City, Vietnam*

This study systematically investigated the influence of sintering temperature on the structure, microstructure, and piezoelectric properties of the transducers. The transducers sintered at 1050, 1100, 1150, 1200, and 1250 °C exhibited a typical tetragonal structure, with the tetragonal and rhombohedral phases coexisting. The disk-shaped transducers sintered at the optimal sintering temperature of 1150 °C for 2 hours displayed a uniform grain structure and achieved the best performance, with a 7.74 g/cm^3 ceramic density, a 472 pC/N piezoelectric coefficient (d_{33}), an 88 mechanical quality factor (Q_m), and electromechanical coupling coefficients k_p and k_t equaling 0.66 and 0.59, respectively. Additionally, based on these results, a cylindrical transducer was successfully fabricated and sintered at 1150 °C for 3 hours, which achieved an effective coupling coefficient (k_{eff}) of 0.26. With these properties, $Pb(Zr_{0.525}Ti_{0.475})_{0.970}Nb_{0.024}Sb_{0.006}O_3$ (PZTNS) piezoelectric transducers showed strong potential for applications in sensors, ultrasonic devices, and underwater acoustic systems. Additionally, this study discussed the agreement between the vibration characteristics of the experimentally fabricated PZTNS ceramics and the simulation program combined with the finite element method.

Keywords: Cylindrical-shaped, Finite element modeling, Sintering temperature, Piezoelectric transducer.

Introduction

Due to their excellent piezoelectric, dielectric, and photoelectric properties, PZT-based piezoelectric materials have attracted significant attention from domestic and international researchers for decades [1-6]. Although PZT-based ceramics exhibit great potential for various applications, the high sintering temperature in the 1200–1350 °C range significantly increases the manufacturing cost. Moreover, PbO evaporation during sintering deteriorates the ceramic properties and causes environmental pollution [7]. PbO evaporation harms the environment, and it promotes abnormal grain growth to limit the material performance and affect the ceramic density [8]. Therefore, reducing the sintering temperature of PZT-based ceramics can address the aforementioned problems and significantly decrease the production cost of materials. Furthermore, this approach may further expand the potential applications of future piezoelectric devices. Adjustments in the composition of PZT ceramics have formed two primary material groups: “hard PZT and “soft PZT. It is well known that materials used for ultrasonic transducer applications should exhibit properties intermediate to those of hard and soft piezoelectric materials. Soft PZT is commonly used in high-sensitivity receiving transducers, high-power pulse emitters, and actuators with large displacement amplitudes [4,9]. Soft piezoelectric materials are relatively easy to polarize and are characterized by a high k_p, a large d_{33}, and a high ε. Consequently, the devices can have improved power efficiency and operating bandwidth [10-12].

The PZT ceramics can be softened by selecting a composition with a Zr/Ti ratio near the morphotropic phase boundary (MPB), substituting isovalent dopants at the A-site, or introducing one or two donor dopants at the *A*- or *B*-site of the crystal lattice [13-15]. Niobium (Nb) has a valence of 5+, and it acts as a donor when introduced into PZT. Additionally, it always substitutes at the *B*-site in the ABO_3 structure. In contrast, antimony (Sb) can exist in +3 and +5 oxidation states, allowing it to substitute at the *A*- or *B*-site. Sb enhances the piezoelectric coefficient but tends to lower the phase transition temperature. Therefore, Nb and Sb co-doping can simultaneously maintain a high piezoelectric coefficient and an elevated phase transition temperature to make the material well-suited for practical applications.

This study introduced Nb and Sb co-doping into PZT to develop a soft ceramic material with enhanced piezoelectric properties, with the aim of fabricating transducers tailored for various devices with corresponding sizes and geometries. This study presented the fabrication process and characterization of the piezoelectric properties of cylindrical transducers based on PZT and PZTNS, with a focus on applications in ultrasonic and

*Corresponding author:
Tel :
Fax:
E-mail: vttung@hueuni.edu.vn; vothantungdhkh@gmail.com

hydroacoustic devices and vibration simulation using the finite element method (FEM). The electromechanical coupling factor or *k*-value of the piezoelectric materials, PZT and PZTNS, was measured using FEM modeling. The *k*-value of both piezoelectric samples was calculated and demonstrated for applications. Additionally, the physical properties of the piezoceramics in the PZT family and of PZTNS were analyzed and compared using the obtained results, and the advantageous properties of new PZTNS material were shown. The obtained results are expected to contribute to fundamental research and practical applications in this field.

Experimental Procedure

The disk-shaped transducer was fabricated with the general formula $Pb(Zr_{0.525}Ti_{0.475})_{0.970}Nb_{0.024}Sb_{0.006}O_3$ (PZTNS), using the conventional solid – state reaction method. The starting materials included in PbO (Korea, 99%), ZrO_2 (Korea, 99%), TiO_2 (Korea, 98%), Nb_2O_5 (Korea, 99.9%), and Sb_2O_3 (Korea, 99.9%). The raw powders were weighed according to the desired stoichiometric ratio and milled with ethanol for 20 hours using a high-energy ball mill machine. The resulting powder was dried, pressed, and calcined at 850 °C for 2 hours. After calcination, the powder was re-milled with ethanol for 20 hours and subsequently dried. Subsequently, 5% polyvinyl alcohol (PVA) was added as a binder to facilitate molding during pressing. The transducer was pressed into a cylindrical shape, followed by sintering at 1050, 1100, 1150, 1200, and 1250 °C for 2 hours with a 5 °C/min heating rate. Ten independently fabricated samples were prepared for each sintering temperature. The reported values correspond to the mean values, and the associated standard deviations were calculated to evaluate the reproducibility and statistical significance of the results.

The crystal structures of the fabricated ceramics were analyzed using X-ray diffraction (XRD, D8 ADVANCE diffractometer). The experiments were performed at room temperature (RT) under Cu-Ka radiation at a 1.5405 wavelength in the 2θ range of 20°–70°, with a step size of 0.02°. The ceramic surface morphologies were examined using scanning electron microscopy (SEM, Hitachi S_4800). The k_p and the Q_m were determined following the resonance method according to the IEEE Standard using an impedance analyzer (LCR HIOKI 3532). A d_{33} meter (YE2730A, Sinocera) was used to determine the piezoelectric constant (d_{33}). Additionally, the ε and tanδ were measured using an LCR meter (HIOKI 3532). The synthesized pellets were pooled in a silicone oil bath at 120 °C by applying a DC electric field (30 kV/cm) for over 30 min. The ferroelectric hysteresis loop was investigated using the Sawyer–Tower circuit. FEM was used to simulate the vibration spectra.

Results and Discussion

The influence of sintering temperature on the physical properties of PZTNS-based disk-shaped transducers

The most critical processing parameters for the fabrication of transducers are the sintering temperature and the annealing duration. After fabrication, the PZTNS-based disk-shaped transducers were sintered at 1050, 1100, 1150, 1200, and 1250 °C for 2 hours (Fig. 1(a)). For the convenience of the investigation, the disk-shaped transducer samples sintered at 1050, 1100, 1150, 1200, and 1250 °C for 2 hours were designated as BT1050, BT1100, BT1150, BT1200, and BT1250, respectively. The ceramic densities of the transducers sintered at 1050, 1100, 1150, 1200, and 1250 °C are presented in Fig. 1.

As shown in Fig. 1(b), the ceramic density of the transducers depended on the sintering temperature. As the sintering temperature increased from 1050 to 1250 °C, the ceramic density gradually increased to reach the maximum value of 7.74 g/cm^3 at 1150 ºC. The ceramic density decreased when the sintering temperature was further increased above 1150 ºC. The ceramic density increased with the rise in sintering temperature, which

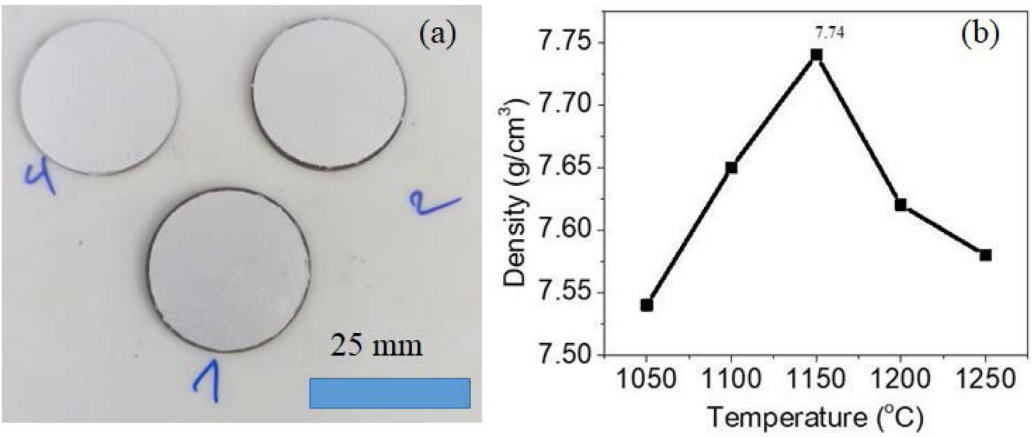

Fig. 1. (a) Disk - shaped transducers; (b) Density of the transducers as a function of sintering temperature.

indicated enhanced densification and reduced porosity. The ceramic density reached a maximum at intermediate temperatures, reflecting optimal sintering and effective particle bonding. Further increase in temperature led to saturation or a slight reduction in the ceramic density, possibly due to PbO volatilization or excessive grain growth. This trend suggested progressive microstructural compactness, followed by degradation mechanisms. A higher ceramic density was directly associated with improved electrical and piezoelectric properties.

The observed density variation trend agreed with the studies on PNN–PZT ceramics, where an optimal sintering temperature achieved the maximum density, which slightly decreased at higher temperatures due to lead loss or abnormal grain growth [16]. Additionally, these studies indicated that high density corresponded to compact microstructure and optimal grain size. The initial linear increase reflected effective mass transport and particle bonding during sintering. Beyond the optimum temperature, defects and PbO volatilization reduced the density [17]. The increase in density with rising sintering temperatures was attributed to enhanced mass diffusion and particle bonding that reduced the porosity and improved compactness. At the optimal temperature, surface energy reduction promoted strong grain bonding and uniform microstructure formation. Excessive temperature could cause PbO volatilization and abnormal grain growth to generate secondary pores and lower the density. Additionally, large grains reduced the grain boundary area to limit further densification, which was similar to the report by Vuong et al. [18].

The XRD patterns of the BT1050, BT1100, BT1150, BT1200, and BT1250 samples are presented in Fig. 2. The XRD patterns indicated that all fabricated transducers exhibited a typical ABO_3 perovskite structure. However, a secondary phase with very low intensity appeared when the transducers were sintered at temperatures above 1150 °C. Within the 2θ range of 20°–70°, all samples displayed a tetragonal structure, which was characterized by a single diffraction peak at approximately 38° and split diffraction peaks at approximately 22°, 31°, 45°, and 55° (Fig. 2(a)). In the 2θ range of 43°– 46°, the diffraction patterns showed a splitting of the (200) peak into $(200)_R$ and $(200)_T$, which indicated the coexistence of rhombohedral and tetragonal phases within the structure (Fig. 2(b)). The magnified region at 43–46 showed peak splitting of the (200)/(002) reflections, suggesting a tetragonal structure near MPB. The increased peak intensity and narrowed full width at half maximum implied grain growth and reduced lattice defects. No evident secondary phase was detected at higher temperatures, indicating perovskite phase stabilization. The slight peak shifts suggested that ionic diffusion and internal stress induced lattice distortion.

The crystal structure improvement with the increase in sintering temperature could be attributed to enhanced ionic diffusion and reduced lattice defects, which promoted the formation of a stable perovskite structure. The ions substituted at the A- and B-sites generated oxygen vacancies and lattice distortions, which altered symmetry and facilitated structural phase transitions. The coexistence of the tetragonal and rhombohedral phases near MPB provided multiple polarization directions, enhancing piezoelectric response and domain switching [19]. Secondary phases or porosity could persist at insufficient sintering temperatures, reducing crystallinity and electrical performance. In contrast, optimal temperature sintering promoted densification and microstructural homogeneity. Therefore, a precise control of the sintering temperature for optimizing structural stability and functional properties was critical.

Furthermore, these observations were consistent with previous studies on PSbN–PZT systems, where a single perovskite phase formed under proper sintering conditions and impurity phases appeared primarily at low temperatures or off-stoichiometric compositions [20]. Additionally, earlier reports indicated the emergence of pyrochlore phases when the Sb/Nb content exceeded

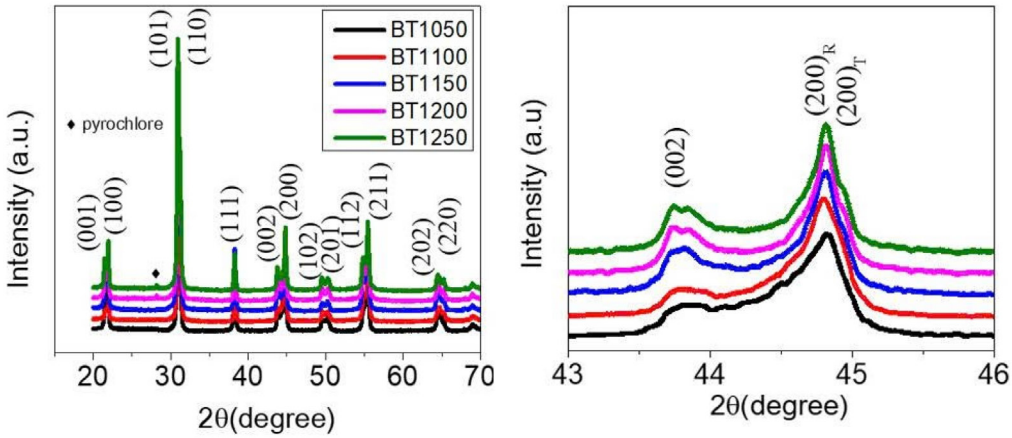

Fig. 2. The XRD patterns of the BT1050, BT1100, BT1150, BT1200, and BT1250 samples sintered at 1050, 1100, 1150, 1200, and 1250 °C, respectively

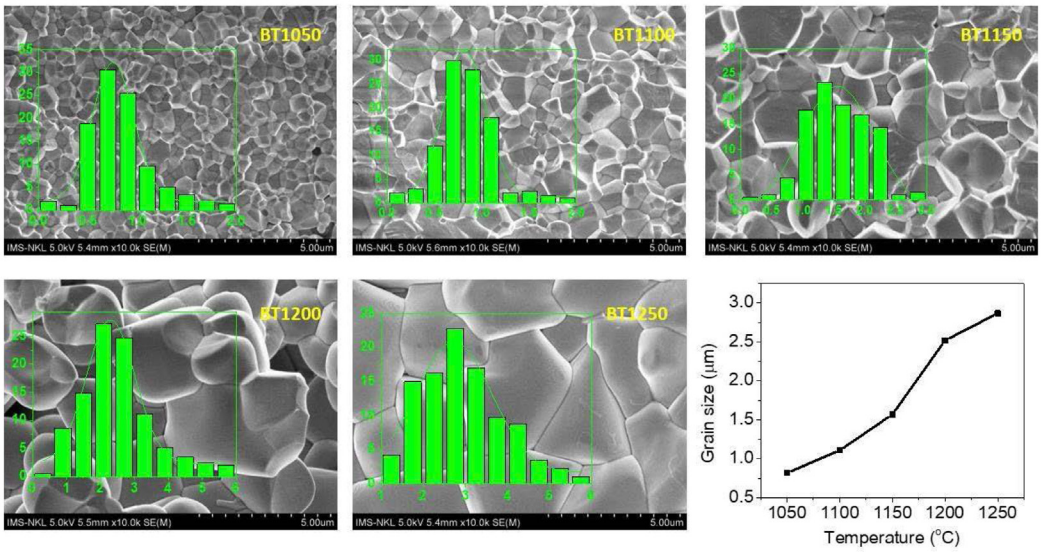

Fig. 3. SEM image of the transducers as a function of sintering temperature.

the solid solubility limit or under inadequate sintering conditions [21]. The (200) peak splitting in the 42–46 region was widely reported as evidence of tetragonal–rhombohedral phase coexistence near MPB. Compared with the samples containing pyrochlore phases, the XRD pattern in this study suggested higher phase purity. Consequently, this implied optimized sintering conditions and compositional control. The improved crystallinity trend agreed well with the referenced literature [18,22].

The effect of sintering temperature on the microstructures of the transducers was investigated using SEM. The SEM results revealed that the microstructure of the transducers strongly depended on the sintering temperature. The average grain size of the samples was determined using the SEM images, and a plot illustrating the dependence of grain size on sintering temperature is presented in Fig. 3. The results indicated a gradually increased grain size with the increase in sintering temperature, which reflected enhanced diffusion and grain boundary mobility at elevated temperatures. At lower sintering temperatures, the grains remained fine and relatively uniform due to incomplete densification. The neck growth and grain boundary migration promoted significant grain coarsening as the temperature increased. The nearly linear trend suggested that normal grain growth dominated the process. At higher sintering temperatures, a further reduction in the grain boundary energy could accelerate grain growth. Therefore, these findings confirmed that sintering temperature critically controlled the microstructure evolution.

The increase in the grain size with sintering temperature was primarily attributed to enhanced atomic diffusion and grain boundary migration, which reduced the free energy of the system. The grain boundary and lattice diffusion became dominant with increased temperatures, which accelerated the boundary movement. At the optimal sintering temperature, the grain size reached a balanced value to ensure high density and effective domain activity. However, excessively high sintering temperatures could induce abnormal grain growth and PbO volatilization, leading to property degradation. Therefore, the precise control of sintering temperature was essential for optimizing the microstructure and piezoelectric performance. The observed grain growth trend was consistent with the results of the study of Mahajan [16]. The grain size increased almost linearly from approximately 0.98 to 2.56 μm. The grain growth was accompanied by improved densification and optimal piezoelectric properties at intermediate sintering temperatures. Based on the results obtained from the density, structure, and microstructure, it could be preliminarily concluded that the optimal sintering temperature for disk-shaped transducers based on PZTNS ceramics was 1150 °C. Accordingly, the influence of sintering temperature on the dielectric and piezoelectric properties of the samples was evaluated using further

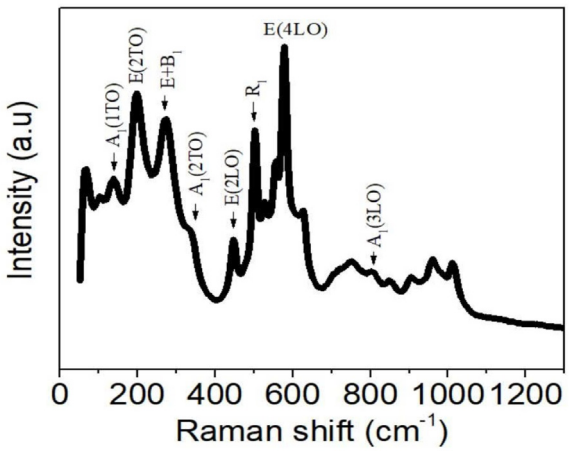

Fig. 4. The Raman scattering spectrum of the PZTNS ceramic sintered at 1050 °C.

investigations.

The Raman scattering spectrum of the PZTNS ceramic sintered at 1150 °C for 2 hours is presented in Fig. 4. The results of group analysis showed that PZT had 12 optical normal (Raman) modes. In the studied frequency range, the major Raman shift peaks were at approximately 140, 205, 270, 330, 430, 580, 680, 740, and 825 cm^{-1}, which fitted well with the vibration modes of A1(1TO), E($2TO_1$), silent (E + B1), A_1(2TO), E(2LO), R_1, E(4LO), R_h, and A_1(3LO), respectively [23,24]. The peak center at approximately 140 cm^{-1} could be assigned to the A_1(1TO) mode vibration [25]. The E($2TO_1$) and silent (E + B1) modes could be assigned to BO_6 rotation, with the silent (E + B1) mode manifesting a mixture of phases with peaks from tetragonal and rhombohedral structures [25]. Zhu et al. noticed that the E($2TO_1$) mode in tetragonal $PbTiO_3$ appeared at 205 cm^{-1} at *RT* [23].

The Raman spectrum of the PZTNS ceramic showed several broad vibration bands in the 0–900 cm^{-1} range, which were characteristic of the perovskite ferroelectric structure. The three primary regions identified were the low-frequency region (0–180 cm^{-1}), the intermediate region (180–400 cm^{-1}), and the high-frequency region (400–900 cm^{-1}). The low-frequency modes were primarily associated with the vibrations of A-site ions in the perovskite lattice, such as Pb^{2+}. The intermediate region corresponded to the bending vibrations of B–O bonds, which involved the Ti–O and Zr–O interactions. Meanwhile, the high-frequency modes were attributed to the stretching vibrations of the BO_6 octahedra (TiO_6 and ZrO_6). The appearance of the broad peaks indicated a certain degree of lattice disorder in the ferroelectric ceramic. Furthermore, these spectral features were consistent with the Raman characteristics commonly observed in PSN-PZT systems [26].

The influence of sintering temperature on the dielectric properties of the transducers at 1 kHz at *RT* is shown in Fig. 5. An increase in the sintering temperature gradually increased the dielectric constant at *RT* but decreased the dielectric loss. At a sintering temperature of 1150 °C, the dielectric constant reached its maximum value of 1686, and the dielectric loss reached its minimum value of 0.018. A further increase in the sintering temperature

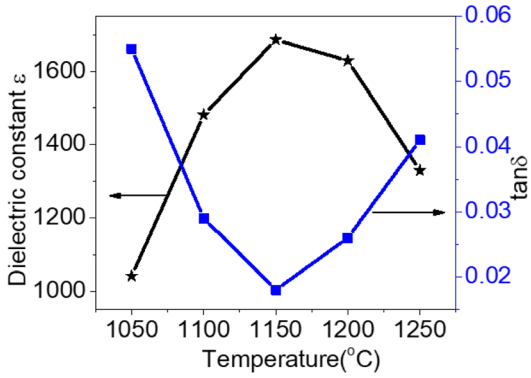

Fig. 5. Dielectric properties of the transducers as a function of sintering temperature.

decreased the dielectric constant and increased the dielectric loss. This behavior could be explained by the grain-size effect and was consistent with the SEM analysis results of the transducers sintered at different temperatures.

The temperature dependence of the ε and tanδ of PZTNS transducers measured at 1 kHz and sintered at 1150 °C for 2 hours is presented in Fig. 6. The dielectric permittivity increased with temperature to reach a maximum at the Curie temperature (T_c), followed by a rapid decrease at higher temperatures. The ε and tanδ values of the PZTNS ceramic measured at 1 kHz were 33135 and 0.045, respectively. The fitting results allowed the determination of the diffuseness of the ceramic. The diffuseness parameter of the sample was 1.67, which clearly indicated the presence of a diffuse phase transition.

The dielectric response of PZTNS ceramics could be attributed to the polarization mechanisms associated with domain wall motion and lattice distortion. Thermal activation enhanced the mobility of ferroelectric domains near T_c, which significantly increased the dielectric permittivity. The substitution of complex ions, such as ($Sb_{1/2}Nb_{1/2}$), on the *B*-site of the perovskite lattice induced local structural distortion and modified the polarization dynamics. Subsequently, this distortion facilitated domain wall movement at moderate temperatures but suppressed

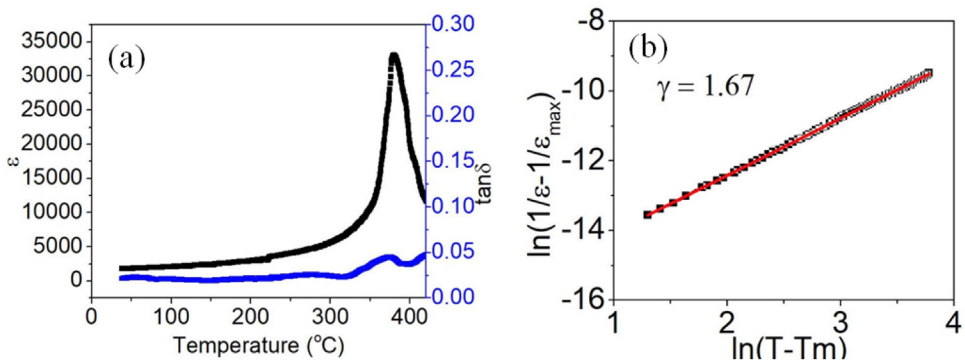

Fig. 6. Temperature dependence of the ε and tanδ at 1 kHz of the PZTNS ceramics.

polarization at higher temperatures when the material entered the paraelectric phase. Similar mechanisms have been discussed for PSN-PZT ceramics, where the B-site ion pairs altered lattice stability and dipole interactions to influence the phase transition and dielectric properties. Overall, the dielectric spectrum of PZTNS followed the typical ferroelectric transition behavior, which was consistent with the previously reported PSN-PZT-based ceramics [27]. Furthermore, Fig. 6 also shows that the T_C temperature of the ceramic is over 350 °C, which is important for temperature stability. In other words, a high phase transition temperature (T_C) enhances the stable operation temperature of the transducers. As is well known, the ferroelectric phase always exists below the T_C of ceramics; the operating temperature of piezoelectric transducers is usually 50-100 °C lower than the T_C temperature [28]. Therefore, these ceramics exhibited good thermal stability, making them suitable for practical applications.

The resonance spectra corresponding to the radial and thickness vibration modes were measured for the transducer samples sintered at 1050, 1100, 1150, 1200, and 1250 °C to investigate their piezoelectric properties, as illustrated in Figs. 7 and 8.The radial resonance spectra were recorded over the 55–90 kHz frequency range with a 0.2 kHz measurement step at a 0.5 V applied voltage using an impedance analyzer (HIOKI 3532). The thickness resonance spectra were measured over the 1–9 MHz frequency range with a 20 kHz step using an impedance measurement system (HP 4193A).

The resonance and anti-resonance frequency pairs corresponding to the maximum and minimum values of impedance (Z) were determined using the resonance spectra. The electromechanical coupling coefficients in the radial mode (k_p) and thickness mode (k_t) for the transducers sintered at different temperatures were calculated based on piezoelectric standards IRE61 and IRE87. The dependence of k_p and k_t, the piezoelectric

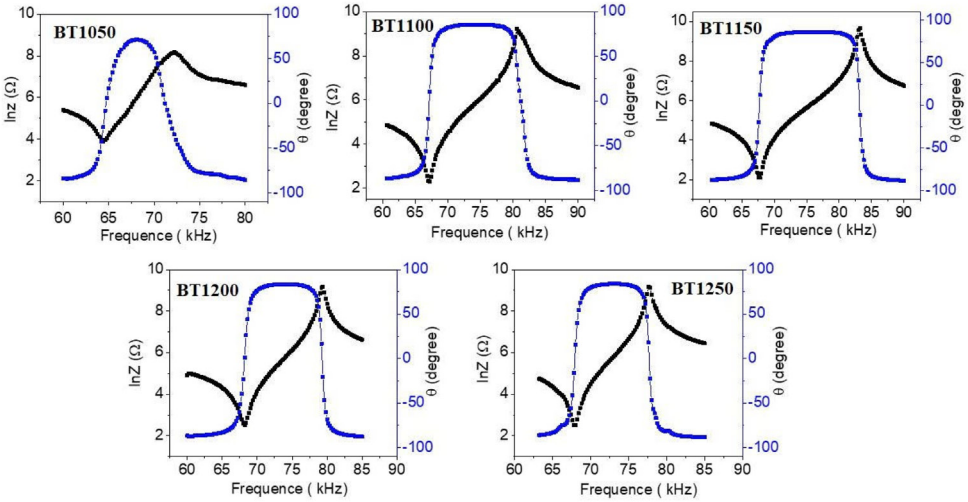

Fig. 7. Radial vibration spectra of the transducers as a function of the sintering temperature.

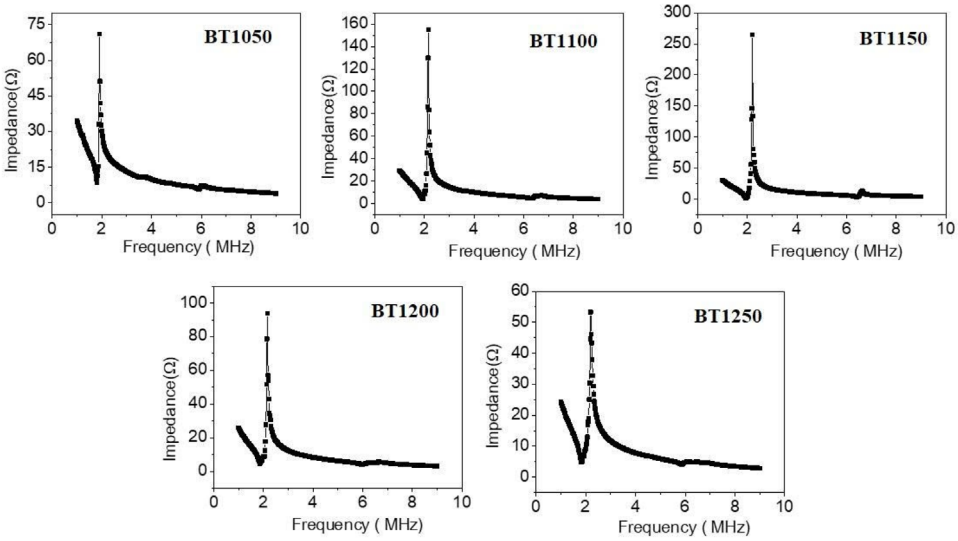

Fig. 8. Thickness-mode vibration spectra of the transducers as a function of sintering temperature.

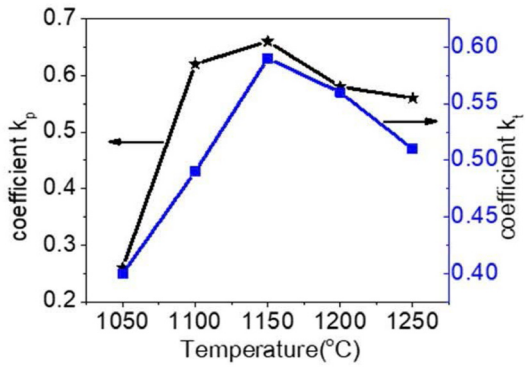

Fig. 9. The dependence of the electromechanical coupling coefficients k_p and k_t on sintering temperature.

coefficient (d_{33} and d_{31}), and Q_m on sintering temperature is presented in Figs. 9 and 10.

The results indicated that the k_p, k_t, d_{33}, d_{31}, and Q_m values of the transducers depended strongly on the sintering temperature. As the sintering temperature increased from 1050 to 1150 °C, the k_p, k_t, d_{33}, d_{31}, and Q_m increased to reach their maximum values of 0.66, 0.59, 472 pC/N, and 88 at 1150 °C, respectively. When the sintering temperature was further increased, these parameters decreased. Additionally, this behavior could be because the transducer exhibited the highest ceramic density and a stable microstructure at 1150 °C, which enhanced ionic motion within the crystal lattice and consequently improved the piezoelectric properties of the material.

The ferroelectric hysteresis loop of the PZTNS ceramic sintered at 1150 °C for 2 hours, which was measured using the Sawyer–Tower method, is shown in Fig. 11. The loop exhibited the typical characteristics of relaxor ferroelectric materials, with a slim hysteresis shape. The coercive field (E_c) and remanent polarization (P_r) determined from the hysteresis loop were 5.69 kV/cm and 36.9 μC/cm^2, respectively. Based on the investigation results obtained for the effects of sintering temperature on the structure, microstructure, and piezoelectric properties of the transducers, it could be concluded that the optimal sintering of the disk-shaped transducers with a 30 mm diameter and based on PZT ceramics co-doped with Nb and Sb occurred at the sintering temperature of 1150 °C and 2 hours.

To provide a more comprehensive overview, several piezoelectric parameters of the samples are summarized in Table 1. The optimal annealing time of the ceramic samples was determined by sintering them at 1150 C and annealing them for 2, 3, and 4 hours. As shown in Fig.

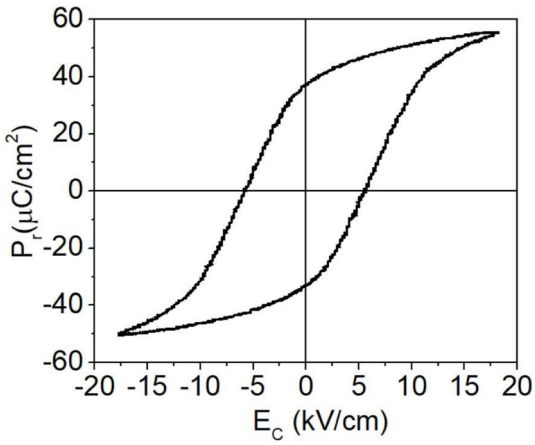

Fig. 11. The ferroelectric hysteresis loop of the PZTNS sample.

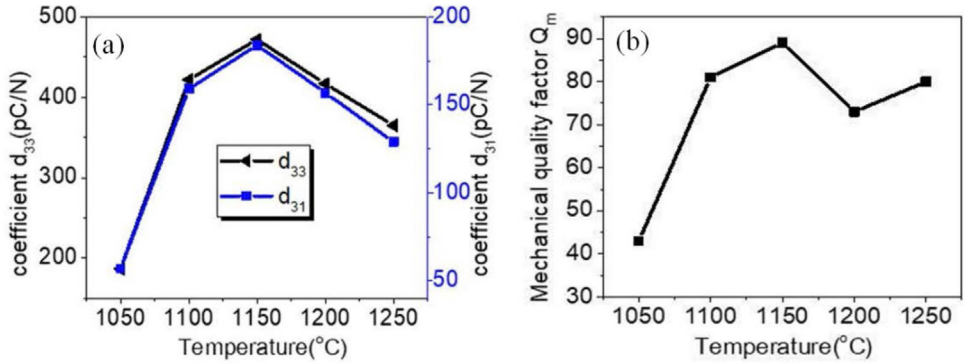

Fig. 10. The dependence of the piezoelectric coefficient d_{33}, d_{31} and the mechanical quality factor Q_m on sintering temperature.

Table 1. Piezoelectric properties of PZTNS-based transducers as a function of sintering temperature.

Temperature	1050 °C	1100 °C	1150 °C	1200 °C	1250 °C
Density (g/cm^3)	7,54 ± 0,030	7,65 ± 0,048	7,74 ± 0,014	7,62 ± 0,072	7,58 ± 0,050
ε	1041 ± 108	1481 ± 27	1686 ± 13	1629 ± 15	1328 ± 139
k_p	0,26 ± 0,028	0,62 ± 0,008	0,66 ± 0,004	0,58 ± 0,012	0,56 ± 0,006
d_{33} (pC/N)	187 ± 13	422 ± 6,2	472 ± 4,2	414 ± 10,8	365 ± 12,8

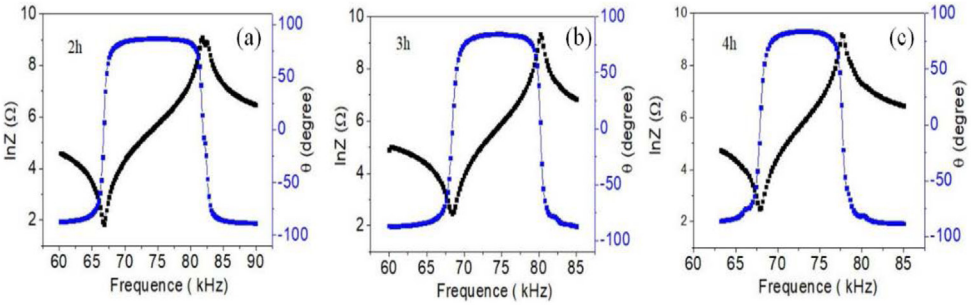

Fig. 12. The radial vibration spectra of the samples.

Table 2. The electromechanical coupling coefficient of the samples.

Sample	f_s (kHz)	f_p (kHz)	k_p
Annealed 2 hours	66.8 ± 0,5	81.8 ± 0,5	0.65 ± 0,005
Annealed 3 hours	68.4 ± 0,5	80.2 ± 0,5	0.59 ± 0,005
Annealed 4 hours	66.4 ± 0,5	76.4 ± 0,5	0.56 ± 0,005

12, the radial vibration spectra were used to determine the Z values at the resonance and anti-resonance frequencies. Based on these Z values, the k_p values of the samples were calculated, as listed in Table 2.

As the annealing time increased, k_p gradually decreased from 0.65 for the sample annealed for 2 h to 0.56 for the sample annealed for 4 h. Furthermore, this could be due to the effect of grain growth at higher sintering temperatures and longer annealing times. Additionally, this result was consistent with the findings reported in a previous study [29]. Based on the results mentioned earlier, it could be concluded that the PZTNS ceramic showed the most optimal properties when sintered at 1150 °C for 2 hours.

Manufacturing and investigation of the piezoelectric properties of a PZTNS piezoelectric ceramic-based cylindrical transducer

The cylindrical probes were fabricated using molds, as described in Fig. 13. Each transducer contained 55–65 g of ceramic powder. After pressing, the cylindrical transducers were sintered at 1150 °C for 3 hours, with the sintering process divided into two stages. The first stage was from *RT* to 300 °C, with a 3 °C/min heating rate. The first stage was because, after pressing to obtain the preliminary shape of the transducer, the samples were inspected to eliminate any cylindrical green bodies that exhibited possible defects. The second stage was from 300 to 1150 °C, with a 5 °C/min heating rate and the temperature of 1150 °C being maintained for 3 hours, followed by cooling down to *RT* at a 5 °C /min rate. Additionally, PbO evaporated at temperatures above 800 °C. Therefore, strict control of PbO evaporation using PbO-saturated atmospheres was a mandatory requirement. If this evaporation were not

Fig. 13. Image of the cylindrical pressing mold.

properly controlled, the fabricated ceramics would have very low electrical resistivity due to the formation of lead vacancies.

The image of the PZTNS ceramics-based cylindrical transducers after sintering at 1150 °C for 3 hours is shown in Fig. 14. The image indicated that cylindrical transducers sintered at 1150 °C for 3 hours had relatively uniform surfaces. Furthermore, the cylindrical transducers were surface-treated, electrode-coated, and polarized to investigate the piezoelectric properties. Poling was conducted at 120 °C for 30 minutes under a 30 kV/cm applied electric field. The image of the cylindrical transducer after electrode-coating is shown in Fig. 15. The frequency-dependent vibration spectrum of the cylindrical transducer was investigated after poling.

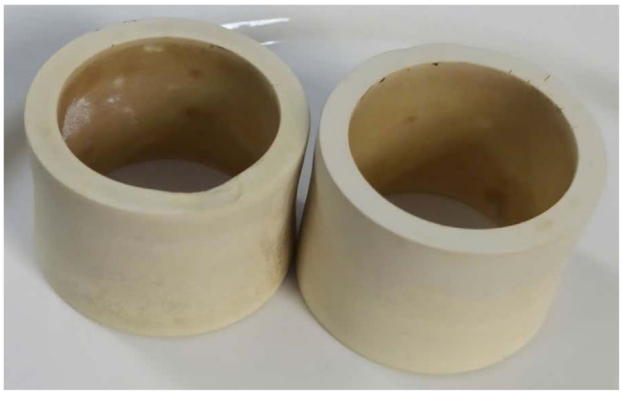

Fig. 14. Cylindrical - shaped transducer after sintering at 1150 °C for 3 hours.

Fig. 15. The image of the cylindrical transducer after electrode coating.

Additionally, the radial vibration resonance spectrum of the cylindrical transducer is shown in Fig. 16.

The impedance dependence was investigated over the 10–120 kHz frequency range, as shown in Fig. 16. The resonance frequency (f_r) and anti-resonance frequency (f_a) were identified from the vibration spectrum of the cylindrical transducer. Accordingly, the f_r and f_a values determined were 56.6 and 58.6 kHz, respectively. In practice, the effective coupling coefficient (k_{eff}), which is used to evaluate the sensitivity of the transducer, is calculated using the following equation [30]:

$$k_{eff} = \sqrt{1 - \frac{f_r^2}{f_a^2}}$$

The k_{eff} value calculated for the PZTNS-based cylindrical transducer was 0.26. A cylindrical transducer was fabricated on a PZT ceramic substrate to compare its

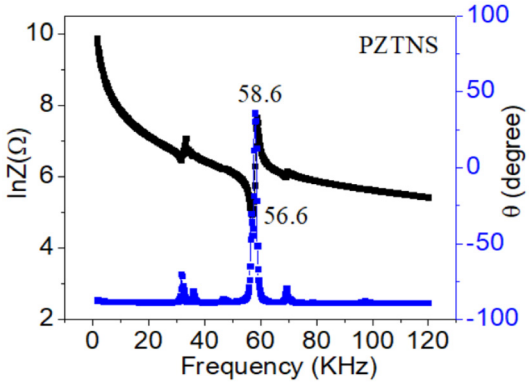

Fig. 16. The vibration resonance spectrum of the cylindrical transducer.

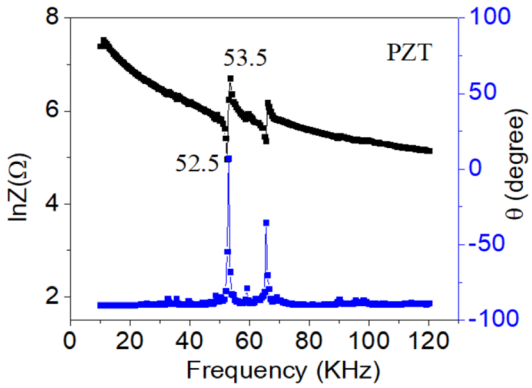

Fig. 17. Variations of impedance log as a function of frequency for vibration mode of PZT.

k_{eff} with that of a PZT-based transducer, and its resonance vibration spectrum was subsequently characterized, as presented in Fig. 17. The frequency-dependent impedance responses within the vibration spectrum of the cylindrical transducer for piezoelectric ceramics belonging to the PZT family are presented in Fig. 17.

As shown in Figs. 16 and 17, within the same frequency range of 10–120 kHz, f_r and f_a of the PZTNS ceramics-based cylindrical transducer shifted toward higher frequencies compared to those of the PZT ceramics-based transducers. Accordingly, the PZT-based transducer exhibited f_r and f_a values of 52.5 and 53.5 kHz, respectively. Accordingly, the k_{eff} values calculated for the transducers based on PZTNS and PZT ceramics were 0.26 and 0.19, respectively. For the convenience of comparison, the measured data are summarized in Table 3.

The difference in the k_{eff} values for the transducers based on PZTNS and PZT ceramics reached up to 31%. Based on these considerations, it was observed that the PZTNS ceramics-based transducer exhibited higher sensitivity than the PZT ceramics-based transducer. Therefore, PZTNS was selected as the fabrication material to satisfy the application requirements of the transducer since its properties were superior compared to PZT. Subsequently, the transducer geometry and the vibration characteristics of the PZTNS material were modeled and analyzed in the following section.

FEM model of the vibration characteristics of a cylindrical transducer

This study employed an axisymmetric three-dimensional (3-D) FEM model to design the geometry of a cylindrical

Table 3. Comparison between the PZT cylindrical transducer and the PZTNS cylindrical transducer.

Characteristic parameters	PZT cylindrical transducer	PZTNS cylindrical transducer
Resonance frequency f_r (kHz)	52.5 ± 0,5	58.6 ± 0,5
Antiresonance frequency f_a (kHz)	53.5 ± 0,5	56.6 ± 0,5
Effective coupling coefficient (k_{eff})	0.19 ± 0,005	0.26 ± 0,005

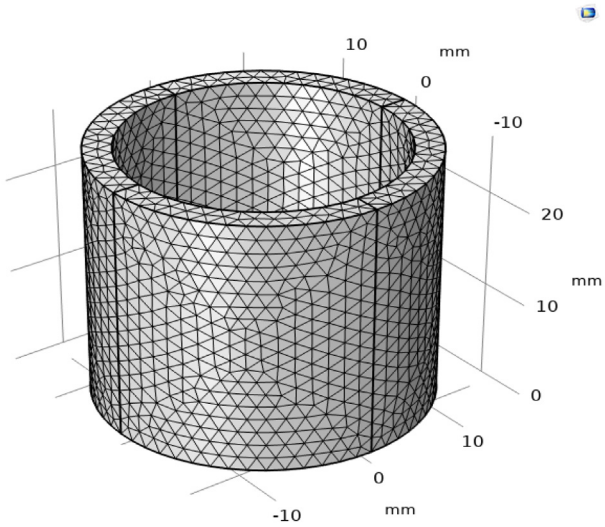

Fig. 18. The fully expanded meshed model of cylindrical - shape transducer.

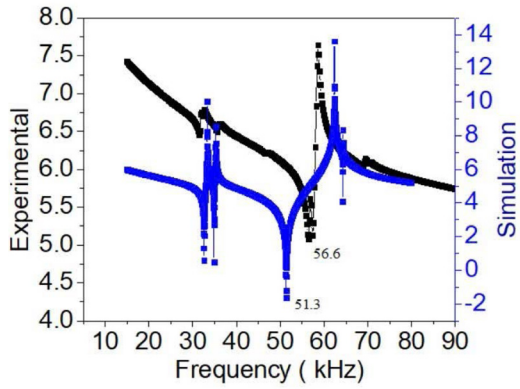

Fig. 19. Comparison between experimental and theoretical normalized frequency spectra of impedance of PZTNS in radial vibration mode.

transducer, with a 26 mm height, a 25 mm inner diameter, and a 30 mm outer diameter. The accurate determination of the resonance frequencies associated with the length, inner diameter, and outer diameter required a sufficiently fine finite element mesh. The FEM model was discretized using a standard meshing tool, with the variations in volumetric, vertex, edge, and boundary elements corresponding to the dimensions of the ceramic samples (Fig. 18). The visualization of the vibration modes generated within the structure at the resonance frequencies could achieve a comprehensive understanding of the resonance characteristics of the cylindrical transducer. A comparison of the normalized frequency spectra of impedance obtained using experimental and simulated methods for PZTNS material is shown in Fig. 19.

The experimentally measured fundamental resonant frequency of the cylindrical PZTNS transducer was approximately 31.4 kHz. However, the resonant frequency predicted using simulation at the fundamental vibration mode was 32.3 kHz. Furthermore, results showed that the appearances of the resonant peaks in the simulation curve were similar to the samples of the materials in the PZT family. The simulated resonant frequencies showed good agreement with the experimental results, with a negligible difference between them. However, the amplitudes of the resonant peaks showed differences, which could be attributed to the limitations in material fabrication and sample preparation and to the inconsistencies between idealized theoretical boundary conditions and actual experimental conditions. Consequently, the FEM model-based numerical results did not coincide exactly with the experimental measurements.

The simulated vibration at the fundamental mode frequency and the 3-D displacement distribution of the cylindrical transducer at different frequencies are shown in Fig. 20. The simulation results showed that the displacement of the transducer varied with the excitation frequency. The maximum displacement occurred at the resonance frequency, where the vibration energy was most efficiently transferred. The displacement amplitude decreased significantly as the excitation frequency deviated from the resonance frequency. The 3-D displacement distribution indicated the expansion and contraction of the piezoelectric elements along the axis of the transducer, which revealed the vibration mode of the system. Consequently, these simulation results provided useful insight for predicting vibration performance and

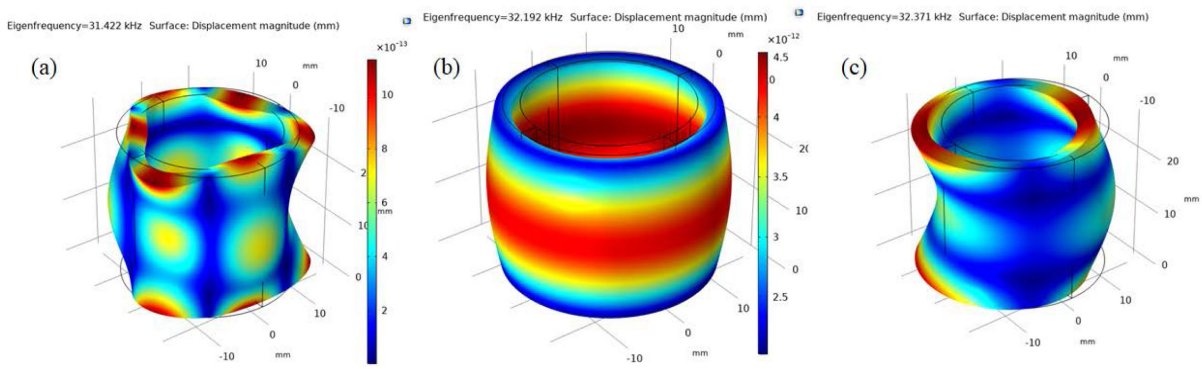

Fig. 20. Displacement of the cylindrical transducer at different frequencies.

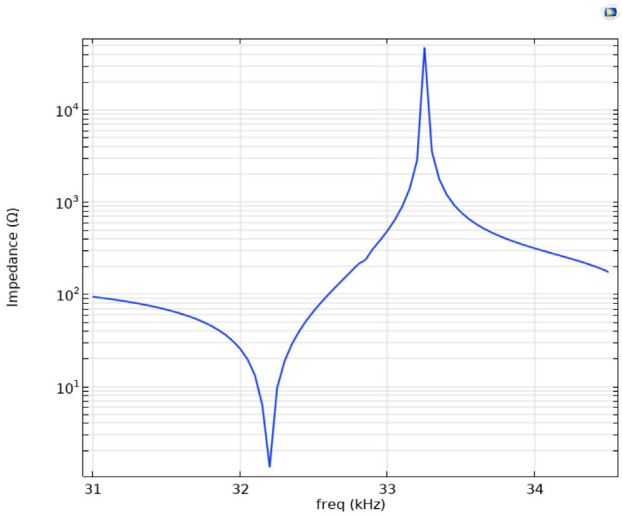

Fig. 21. Resonance spectrum of the cylindrical transducer

optimizing the transducer design.

At 32.192 kHz, the outer boundary of the cylinder exhibited larger displacement values, but the central and upper regions of the cylinder showed smaller displacement values. Therefore, this indicates that the vibration energy was primarily concentrated along the outer wall of the transducer. Such a distribution was characteristic of a bending vibration mode of the cylindrical structure. The finite element simulation results showed a non-uniform displacement distribution on the cylindrical transducer surface at an eigenfrequency of approximately 32.371 kHz and 31.422 kHz. The upper and lower edges of the cylinder showed larger displacement amplitudes, as represented by the red and orange regions. In contrast, the central region of the cylindrical wall exhibited smaller displacement values, as indicated by the blue areas. Consequently, this displacement pattern suggested the presence of a bending vibration mode in the cylindrical structure, causing the sidewall to deform laterally.

Based on the analysis mentioned earlier, the impedance spectrum of the cylindrical transducer as a function of frequency was simulated, as presented in Fig. 21. As shown in the impedance spectrum of the cylindrical transducer in the frequency range from approximately 31 to 34.5 kHz in Fig. 21, the minimum impedance point observed around 32.2 kHz corresponded to f_r of the transducer. At this frequency, the electrical impedance reached its lowest value because the electrical energy was efficiently converted into mechanical vibration. A maximum impedance peak appeared at approximately 33.2 kHz, corresponding to f_a. The separation between f_r and f_a reflected the electromechanical coupling behavior of the transducer and could be used to determine k_{eff}. Accordingly, the calculated k_{eff} value for the cylindrical transducer obtained from the simulation was 0.24. Thus, compared with the experimental results, k_{eff} obtained from simulation showed only a small difference, which indicated a good agreement between the simulation and experimental results.

A quantitative comparison between the finite element simulation and experimental measurements is summarized in Table 4. The simulated resonance and antiresonance frequencies are 32.2 and 33.2 kHz, respectively, while the corresponding experimental values are 31.4 and 32.3 kHz. The percentage errors are 2.55% and 2.79%, respectively, indicating good agreement between the finite element model and the experimental observations. The slight discrepancies may be attributed to uncertainties in material parameters, fabrication tolerances, and simplifications adopted in the numerical model.

The higher effective electromechanical coupling coefficient of the PZTNS cylindrical transducer indicates a more efficient conversion between electrical and mechanical energy. This improvement can enhance transmitting and receiving sensitivity, broaden the operational bandwidth, and reduce power losses. Consequently, the developed transducer is expected to provide superior performance in underwater acoustic applications, such as sonar systems, underwater communication, and hydrophones, where high sensitivity and energy efficiency are critical. In addition, the enhanced coupling characteristics make the transducer attractive for high-power ultrasonic devices, non-destructive testing (NDT), and ultrasonic sensing systems. Therefore, the PZTNS cylindrical transducer offers significant practical advantages over conventional PZT transducers in applications requiring high electroacoustic conversion efficiency and improved acoustic performance.

Conclusion

This study used the conventional ceramic method to successfully fabricate disk-shaped transducers based on PZTNS ceramics. The transducers sintered at the optimal sintering temperature of 1150 °C for 2 hours exhibited the best performance, with ceramic density, d_{33}, k_p, and k_t equal to 7.74 g/cm^3, 472 pC/N, 0.66, and 0.59, respectively. Additionally, based on these results, a cylindrical transducer was successfully fabricated and sintered at 1150 °C for 3 hours, achieving k_{eff} = 0.26. The finite element model integrated with the simulation

Table 4. Comparison between finite element simulation and experimental result for the PZTNS cylindrical transducer.

Characteristic parameters	FEM simulation (kHz)	Experiment (kHz)	Error (%)
Resonance frequency f_r	32.2	31.4	2.55
Antiresonance frequency f_a	33.2	32.3	2.79

framework demonstrated excellent agreement with experimental data in the investigation of the properties of the new material systems. Consequently, these results were expected to provide a foundation for future research, in fundamental studies and practical applications, particularly in ultrasonic and hydroacoustic devices.

Acknowledgements

This research was funded by Hue University under Hue University Science and Technology Project number DHH2025-01-230.

Data availability: The raw data supporting the conclusions of this articlewill be made available by the authors on reasonable request.

Conflict of interest: The authors declare that they have no conflict of interest.

References

1. H. Jaffe, J. Am. Ceram. Soc. 41[11] (1958) 494-498.
2. C. Tapaonoi, S.T.S. Tashiro, and H.I.H. Igarashi, Jpn. J. Appl. Phys. 33[9S] (1994) 5336.
3. S. Zhao, H. Wu, and Q. Sun, Mater. Sci. Eng. B 123[3] (2005) 203-210.
4. A. Nechibvute, A. Chawanda, and P. Luhanga, Int. Sch. Res. Notices 2012[1] (2012) 921361.
5. Y. Xu, in "Ferroelectric Materials and Their Applications" (Elsevier, 2013).
6. J. Du, H. Yang, Z. Mu, C. Yang, J. Yan, and Y. Chen, J. Electroceram. (2024) 1-10.
7. L.D. Vuong, P.D. Gio, N.D.V. Quang, T.D. Hieu, and T.P. Nam, J. Electron. Mater. 47[10] (2018) 5944-5951.
8. A. Kumar, S.R. Emani, K. James Raju, J. Ryu, and A. James, Energies 13[23] (2020) 6457.
9. H. Zheng, I.M. Reaney, W.E. Lee, N. Jones, and H. Thomas, J. Am. Ceram. Soc. 85[9] (2002) 2337-2344
10. M.-K. Zhu, P.-X. Lu, Y.-D. Hou, H. Wang, and H. Yan, J. Mater. Res. 20[10] (2005) 2670-2675.
11. H. Zhang, J. Shen, J. Tian, J. Zhou, and W. Chen, Ferroelectrics 491[1] (2016) 15-26.
12. S. Dursun, A.E. Gurdal, S. Tuncdemir, and C. Randall, Sens. Actuators A Phys. 286 (2019) 4-13.
13. V. Kalem, İ. Çam and M. Timuçin, Ceram. Int. 37[4] (2011) 1265-1275.
14. S. Eitssayeam, P. Jarupoom, and G. Rujijanagul, Ferroelectrics 451[1] (2013) 48-53.
15. S.M. Hu, G.G. Peng, and D.Y. Zheng, Appl. Mech. Mater. 700 (2015) 121-124.
16. S. Mahajan, O. Thakur, and C. Prakash, Def. Sci. J. 57[1] (2007) 23-28.
17. L.D. Vuong, N. Van Thinh, D.V. On, and V.T. Tung, J. Mater. Sci. Mater. Electron. 36[4] (2025) 284.
18. L.D. Vuong, N.Q. Lich, N.X. Cuong, V.Q. Nha, N.D. Nhat, L.D. Hieu, L.P. Son, H.T.T. Linh, N.H. Chuc, T.N.A. Tuyen, T.N. Dat, and P.-C. Wei, Mater. Res. Express 10[10] (2023) 105701.
19. D.A. Quang and L.D. Vuong, J. Sci. Adv. Mater. Devices 7[2] (2022) 100436.
20. J. Chen, Z.-Z. Du, Y.-T. Yang, and H. Hu, Ceram. Int. 47[11] (2021) 15195-15201.
21. Z. Zhuo, Z. Ling, and Y. Liu, J. Mater. Sci. Mater. Electron. 29 (2018) 9524-9530.
22. N. Van Thinh, T. Van Chuong, T.N. Dat, and V.T. Tung, J. Ceram. Process. Res. 24[3] (2023) 478-485.
23. M.K. Zhu, P.X. Lu, Y.D. Hou, X.M. Song, H. Wang, and H. Yan, J. Am. Ceram. Soc. 89[12] (2006) 3739-3744.
24. Y.-D. Hou, L.-M. Chang, M.-K. Zhu, X.-M. Song, and H. Yan, J. Appl. Phys. 102[8] (2007).
25. P. Kour, S. Pradhan, P. Kumar, S. Sinha, and M. Kar, Appl. Phys. A 122[6] (2016) 591.
26. S. Huang, J. Zeng, L. Zheng, Z. Man, X. Ruan, X. Shi, and G. Li, Ceram. Int. 46[5] (2020) 6212-6216.
27. Z. Zhuo, Z. Ling, and Y. Liu, J. Mater. Sci. Mater. Electron. 29[11] (2018) 9524-9530.
28. W. Liu, T. Zheng, Z. Zhou, Y. Ding, Y. Qin, Z. Fu, X. Ruan, Z. Gao, X. Lv, and J. Wu, Nat. Commun. 16[1] (2025) 1527.
29. S. Sangawar and B. Praveenkumar, Ferroelectrics 517[1] (2017) 66-74.
30. J. Kim and J. Lee, Sensors 20[7] (2020) 1952.